Development of a Current Sheet in the Wake of a Fast CME

A.G. Ling

Atmospheric Environmental Research, 2201 Buena Vista Drive SE, Suite 407, Albuquerque, NM 87106, USA; aling@aer.com

D. F. Webb

Institute for Scientific Research, Boston College, 140 Commonwealth Ave., Chestnut Hill, MA 02467, USA; david.webb@bc.edu

J. T. Burkepile

High Altitude Observatory/National Center for Atmospheric Research, Boulder, CO 80307, USA; iguana@ucar.edu

E. W. Cliver

Space Vehicles Directorate, Air Force Research Laboratory, Sunspot, NM 88349, USA; ecliver@nso.edu

ABSTRACT

A bright ray that developed in the wake of a fast coronal mass ejection (CME) on 2005 September 7 presents a unique opportunity to study the early development and physical characteristics of a reconnecting current sheet. Polarization brightness images from the Mk4 K-Coronameter at the Mauna Loa Solar Observatory (MLSO) are used to determine the structure of the ray along its axis low in the corona as it progressed outward. Coverage of the early development of the ray out to $\sim$1.3 $R_\odot$ for a period of $\sim$27 hours after the start of the event enables for the first time in white light a measurement of a CME current sheet from the top of the arcade to the base of the flux rope. Measured widths of the ray are combined to obtain the kinematics of the upper and lower "Y" points described in reconnection flux-rope models such as Lin and Forbes (2000). The time dependence of these points are used to derive values for the speed and acceleration of the growth of the current sheet. We note the appearance of a large structure which increases in size as it expands outward in the early development of the ray, and an apparent oscillation with period of $\sim$0.5 hour in the position angle of the ray.

Subject headings: Sun: coronal mass ejections (CMEs) — Sun: corona

1. Introduction

The most energetic solar and interplanetary disturbances are coronal mass ejections (CMEs) in which plasma and magnetic fields are expelled from the Sun into space, on time scales of tens of minutes to hours. CMEs result from a major restructuring of the corona. During such events, magnetic fields and plasma are expelled from the Sun causing dramatic changes in the coronal medium both within and around the erupting volume.

Current sheets (CSs) are important signatures of magnetic reconnection during the eruption of CMEs. Reconnection can play an important role in CME dynamics by removing overlying loops that would otherwise constrain the CME plasma and by providing an upward force in the form of the reconnection outflow. Large-scale CSs have now been identified in white light (WL) coronagraph images of CMEs as narrow rays trailing the outward-moving CME core, and in ultraviolet spectra as narrow, bright, high temperature features.

Essentially all CME models predict the formation of a CME CS underneath the erupting magnetic flux rope (e.g., see Lin and Forbes 2000) as shown schematically in Figure 1. The so-called "standard" flare model has been developed and refined over the last several decades (e.g., Švestka & Cliver, 1992; Shibata et al., 1995; Lin & Forbes, 2000; Lin, 2004 - Figure 1; Chen, 2011). In this model a stressed magnetic arcade that may contain a core magnetic flux rope begins to rise. A neutral CS, i.e., a surface separating fields of opposite magnetic polarity, develops beneath it as external pressure causes oppositely directed magnetic field lines to converge and reconnect. The faster the eruption proceeds, the higher the rate at which new field lines accumulate at the CS. Such post-eruption CSs should be distinguished from the CSs which could exist before the eruption in some flare and CME models. Some of the liberated energy heats and accelerates the CME plasma, adding mass and magnetic flux to it. Energy is also directed downward in the form of shock waves, energetic particles and/or rapidly moving plasma. This energy can heat the low-lying or reconnecting magnetic loops and travel down the loops to the chromosphere, producing a Hα flare.

The WL rays seen by coronagraphs behind CMEs (e.g., Ko et al. 2003; Webb et al. 2003; Vršnak et al. 2009) provide important observational evidence supporting the existence of CME CSs. The rays are formed in the wake of CMEs, can extend to several solar radii, and persist from several hours to a day or more. Such rays are not quiescent but often exhibit dynamics such as propagating blobs through the ray (e.g., Riley et al. 2002; Sheeley & Wang 2007) that could result from the tearing mode instability leading to reconnecting islands in a CS. Several characteristics of WL rays trailing fast CMEs include flux rope-like structures with concave-outward shapes at the base of a CME, rays brightening and elongating with time, propagating blobs, and apparent movement in position angle.

The disconnection of magnetic field lines following CMEs is an important aspect of a class of eruptive flare models; some kind of disconnection appears necessary to prevent the buildup of the net interplanetary magnetic flux. However, until the launch of the SOHO LASCO coronagraphs, the observation of events at the Sun providing evidence of magnetic disconnection, such as concave-outward structures (e.g., Illing and Hundhausen, 1986; Cliver, 1989; McComas et al. 1991) had been relatively rare. Kahler and Hundhausen (1992) and Webb and Cliver (1995) studied the structures trailing CMEs and found reforming streamers with rays and concave outward (C-O) features. Webb et al. (2003) used a Solar Maximum Mission (SMM) CME catalog to measure rays trailing C-O CMEs. They found that rays provide observational evidence of magnetic reconnection/disconnection during CME evolution, and address the problem of excessive interplanetary magnetic flux buildup. Their analysis indicated that rays followed at least ∼10-20% of all SMM CMEs and had lifetimes of ∼8 hours. Evidence of magnetic reconnection during CME onset via a stretched current sheet was established which supports some 2-D CME reconnection models such as the Lin and Forbes (2000) model and the Linker et al. (2001) MHD model. With the advent of the more sensitive LASCO coronagraphs, St. Cyr et al. (2000) found that 36%, and possibly as high as 48%, of LASCO CMEs exhibited trailing concave-outward features.

CS structures have been observed at other wavelengths as well; especially relevant are those observations in the low corona near the surface. There, observations of cusp-shaped loops and super arcade downflows (SADs) above eruption sites by the Yohkoh Soft X-ray Telescope (SXT) (Hiei et al. 1993) and Hinode X-ray telescope (XRT) have provided further support for post-CME reconnection over long-duration flares and the existence of post-eruption current sheets (Shibata 1999; McKenzie & Hudson 1999; Innes et al. 2003; Asai et al. 2004; Sheeley et al. 2004; Savage et al. 2010). The SADs are down flowing voids that have been observed above post-CME flare arcades. SADs have trajectories which slow as they reach the top of the arcade, consistent with post-reconnection magnetic flux tubes retracting from a reconnection site high in the corona until they reach a lower-energy magnetic configuration. In the Cartwheel event of 2008 April, Savage et al. (2010) measured the width of the CS to be about 4-5$\times 10^3$ km, and showed that SADs can also appear as shrinking loops rather than down-flowing voids. In that event, for the first time both the CS and the outgoing CME were imaged in soft X-rays and followed into the LASCO C2 field of view.

Sui & Holman (2003) first discussed a hard X-ray event observed by the Reuven Ramaty High Energy Solar Spectroscopic Imager (RHESSI) that showed a compact X-ray source above the top of a roughly vertical CS in which magnetic reconnection was occurring. Subsequently, Sui et al. (2005), Saint-Hilaire et al. (2009) and others analyzed similar events in which the coronal sources appeared to move both downwards and outwards with time. The hard X-ray emission indicates a very hot source, ∼10-100 MK, with the outgoing blob

associated with the magnetic X-point where oppositely-directed field lines are reconnecting. The downward source is likely hot plasma from the most-recently reconnected arcade loops that are shrinking (Švestka et al. 1987), as well observed in the soft X-ray observations. CSs have also been observed by the Solar Dynamics Observatory (SDO), especially in the Atmospheric Imaging Assembly (AIA) 131 Å channel, both as rays when viewed edge on (Reeves & Golub 2011), and as fans when viewed face-on (Savage et al. 2012; Warren et al. 2011). In these events, the AIA 131 Å channel may be imaging emission from Fe XXI, with a temperature of about 11 MK (O'Dwyer et al. 2010).

Bright narrow features with enhanced temperatures (3-6 MK), densities ($\sim 5 \times 10^7$ cm^{-3} at 1.5 $R_\odot$) and abundances of elements with low first ionization potentials (FIPs) were observed with the UVCS following both slow (Ciaravella et al. 2003) and very fast (Ko et al. 2003; Lin et al. 2005) CMEs. Several studies (Yokoyama et al., 2001; Simnett, 2004; Sheeley & Wang, 2007; Vršnak et al., 2009; Savage et al., 2010) identified bi-directional flows in SOHO and Hinode images moving away from a common point in the low to mid-corona that were interpreted in terms of reconnecting CSs. Ciaravella & Raymond (2008) were the first to combine UVCS and WL data to derive both the density and thickness in a CS, rather than assuming one to estimate the other. Recently, Ciaravella et al. (2013) analyzed a sample of coronal rays detected both in WL, from a LASCO CME-ray catalog, and with ultraviolet spectra from UVCS. The sample revealed a wide range of temperatures with hot, coronal and cool rays. Ciaravella et al. (2013) found that about 18% of the WL rays had very hot gas (e.g., with Fe XVIII emission at ∼6 MK), while about 23% contained cold gas (e.g., with C III or O V emission at 10^5 K) that they attributed to cool prominence material draining from the CME core. Coronal CSs are places where one could expect higher heating rates and, therefore, higher temperatures. In SOHO ultraviolet spectra, CSs have been identified as narrow regions of very hot (>3 MK) plasma seen with the UVCS (Kohl et al. 2006) between flare loops and CME cores (e.g., Ciaravella et al. 2002; Ko et al. 2003; Raymond et al. 2003; Bemporad et al. 2006; Lin et al. 2007; Ciaravella & Raymond 2008), or as hot gas with very large line widths above flare loops observed by the Solar Ultraviolet Measurements of Emitted Radiation (SUMER) (Innes et al. 2003; Wang et al. 2007). Narrow band EUV images also show hot gas in CSs above the limb, notably the Transition Region and Coronal Explorer (TRACE) images of Innes et al. (2003) and those mentioned above with SDO.

A key element missing from the WL description of CME-rays is observations of the initial stages of the formation of the CS behind the erupting CME. One reason for this is the lower part of the CS and its connecting arcade lie low in the corona, well below the heights of the occulting disks of earlier spaceborne coronagraphs. The MLSO K-coronameters have continually improved in resolution at low heights. The current Mk4 coronameter covers a region from the edge of the occulting disk at 1.08 $R_\odot$ out to 2.86 $R_\odot$. The bright ray which

developed in the wake of a fast CME on 2005 September 7 presents a unique opportunity to study the evolution and physical characteristics of an erupting current sheet, because the ray was observed during its formation and development. Coverage of the early development of the ray out to ∼1.3 $R_\odot$ for a period of ∼**27** hours after the start of the event enables a first time measurement of a CME CS from the top of the arcade to the base of the flux rope.

The source region of the September 7 event, named NOAA active region 10808 when it appeared on the visible east limb on September 6, was likely associated with a number of fast halo CMEs from late August to September 5. After its arrival on the visible disk, this region produced ∼25 M-class, and 10 X-class flares over the next ten days. The flare associated with the CME for this event was the last extremely energetic flare of solar cycle 23 (optical class 3B; peak SXR flux >X17, saturating the GOES instrument). The Sun has yet to produce a flare of such X-ray magnitude during the current cycle, 24, at the time of this writing. The reported Hα and X-ray start, peak and end times were 17:24, 17:28 and 18:47 UT and 17:17, 17:40 and 18:03 UT, respectively, with disk locations of S06E89 and S11E77, respectively, in active region 10808 (Solar Geophysical Data, 2006). The event produced strong radio emission and type II and IV radio bursts commencing at 17:38 UT. Despite its location on the east limb, a >100 MeV SEP event was observed at Earth. The SEP caused a strong (NOAA-S3) radiation storm and the associated flare led to a severe (NOAA-R4) radio blackout, affecting communication and navigation systems[1] (W. Murtagh, 2011, private communiation).

Figure 2 shows the height-time plots of the leading edges of the bright CME rim and of the void which is possibly related to the erupting prominence. The linear-fit leading edge speed of 2490 km/s was the fastest ever observed by the MLSO Mk4 K-coronameter (Elmore et al. 2003). The CME was so fast that only 2-3 measurements of each structure were possible within the field of view (see the Mk4 movie accompanying the electronic version of this paper). A number of associated phenomena accompanied the CME, including a fast erupting prominence at the limb (EPL) and a He I 10830 Å surface wave. The other movies accompanying this paper show the EPL as observed with the Polarimeter for Inner Coronal Studies, and the surface wave as observed with the Chromospheric Helium-I Imaging Photometer. This event permits the study of the formation of an eruptive current sheet low in the corona during the initial stages of development. SOHO was not operating during this period, so the MLSO observations are the only white light data available of the CME and its current sheet. There was a LASCO data gap from September 7, 11:00 UT to September 9, 12:21 UT due to SOHO station keeping and momentum management maneuvers (K. Schenk,

[1]see http://www.swpc.noaa.gov/NOAAscales for a description of the NOAA space weather scales.

2012, private communication).

2. Analysis

2.1. Image Processing

Polarization brightness images from the Mk4 K-coronameter were used in the analysis presented in this work. The Mk4 white light images cover a wavelength range from 700 to 950nm and extend a region of the corona from 1.08 $R_\odot$ to 2.86 $R_\odot$ Nominal observing times are from 17:00-02:30 UT, weather permitting. The Mk4 is an upgrade to the Mk3 K-coronameter that operated from early 1980 through 1999 (Fisher et al. 1981). The Mk4 began operations in 1998 October and overlapped Mk3 for about a year. It uses a 1-D CCD detector to scan the low corona every 1/2° in azimuth, building up a 360° image every 3 minutes. It has a plate scale of 4.855″/pixel, an average measurement uncertainty of ±15%, and a noise level of 4x10$^{-9}B/B_\odot$. An example of an Mk4 image is shown in Figure 3.

MLSO data are available during the intervals from September 7, 17:04 - 19:42 UT, September 8, 00:26 - 02:30 UT, and September 8, 18:17 - 20:08 UT. No data are available for the intervening intervals due to nighttime or clouds. No MLSO data are available from September 9-11. Four types of images are available for analysis: white light polarization brightness data in polar and rectangular coordinates, and white light vignetted data in polar (Figure 3) and rectangular (Figure 4) coordinates. The vignetted data are useful for visual inspection of features but cannot be used for determining absolute quantities such as densities due to the offset applied to the gradient in the radial brightness. Vignetted Mk4 white light polarization brightness images in rectangular coordinates exhibiting the development of the post-CME ray of 2005 September 7 are shown in Figure 4 for nine representative times. In this figure, and hereafter, whenever a time is given associated with an image, that time is understood to be the time of the start of the scan with the scan taking 3 minutes to complete. However, the times associated with measurements of individual pixels along the ray have been corrected for those locations (see Sec. 2.2). The first observation of the white light CME front was at 17:34 UT, before the X-ray peak and onset of the type II burst. The images at 17:34 and 17:36 UT show the classic 3-part CME structure, with a leading circular front followed by a dimmer void with a bright core. The bright core is likely the prominence. This appears circular, or may be a flux rope, as seen at 17:39 and 17:42 UT. The bright, sharp feature to the south at 17:36 and 17:39 UT is located at the angle where the scan started and ended 3 minutes later. The discontinuity in the structure is due to the motion of the CME during the 3-minute scan periods. Figure 2 shows height-time measurements of the loop leading edge of the CME at times 17:36:54 and 17:37:08 UT and of the prominence

structure observed at times 17:36:54, 17:37:08, and 17:42:45 UT, superposed on the GOES X-ray light curve. The CME onset appears to have been ∼10 minutes after the rapid rise in X-rays. The CME can be seen at 17:39:54 UT at a position angle of ∼ 100°. At 17:45:49 UT a large part of the CME has left the field of view and by 17:54:40 UT the formation of the ray can be clearly seen. The remaining images show little movement of the ray over the time range considered, but some motion of the streamer at ∼ 150° can be observed (also see the accompanying Mk4 movie). The analysis for determining the width of the ray was done using the polar coordinate images of size 720 x 384 pixels corresponding to a resolution of 0.5°/pixel and 196.2 pixels/$R_\odot$ for the position angle and height, respectively.

The first step in the analysis was to isolate the ray in each image from the other features. This was done by placing a 4-sided polygon around the ray on each of the vignetted images, an example of which is shown in Figure 3. The polygons for each image were then applied to the corresponding non-vignetted images with only the data contained within the polygon boundaries subjected to analysis. For a given non-vignetted image, slices of data across the width of the polygon at each y-pixel (height along the ray and above solar limb) were used to determine the width of the ray at that y-pixel value. An example of this process is illustrated in Figure 5 which shows the pixel intensity as a function of the x-pixel (position angle from solar north) value at a given y-pixel value for the non-vignetted image of 2005 September 7, 19:01:00 UT. The width of the ray was determined by fitting the data to a Gaussian plus quadratic background, subtracting the background from the data, and fitting the result to a Gaussian plus quadratic background. A quadratic background was used to accommodate cases in which a linear background proved insufficient. The second fit was done to verify that the background was sufficiently represented by a quadratic function. The full width at half maximum (FWHM) from the second fit was taken as the width of the ray. The process was performed at all y-pixel values for which a fit could realistically be obtained. At large y-pixel values the background became comparable to the intensity of the ray, making a width determination impractical. This can be seen in Figure 5 where the background varies by 2 orders of magnitude over the length of the ray and has larger variation at large y-pixel values. The range of x-pixels over which to attempt a fit to the data was determined by visual inspection for each fit separately. The maximum y-pixel values over which a fit could be performed was time dependent, ranging from 71 (1210″ or 1.27 $R_\odot$) at the early development of the ray (2005 September 7, 17:39:54 UT) to 245 (2055″ or 2.16 $R_\odot$), the time when the ray was most clearly discernable (2005 September 7, 19:10:38 UT).

After the FWHM values in pixel units were determined for a given image at all appropriate y-pixel values, the results were used to determine the behavior of the ray width along its axis according to the following procedure. The locations of the peaks from the Gaussian fits were converted to position angles and the y-pixel values were converted to a

distance from Sun center in units of solar radius using the image parameters contained in each image. Since the ray makes a non-radial angle to the surface of the Sun and exhibits curvature along its path, it was necessary to obtain an empirical relationship between the position angle and the distance from Sun center of the points along the ray axis in order to quantify the distance along the ray axis. The position angles of the peak locations were fit to a 3rd order polynomial in distance from Sun center and points outside of 2 standard deviations of the mean were eliminated from consideration in all subsequent analysis prior to a second fit. The fit parameters resulting from the second fit were used to extend the fit to 1 $R_\odot$ and a third fit was done by repeating the second fit with the addition of this point. The results of the third fit were used to determine the distance between each point which were then summed from the point at 1 $R_\odot$ to yield the distance along the ray axis in units of solar radius. From the geometry of the ray shown in Figure 6 the angle θ between the center of the ray and the edge of the ray is

$$\theta = \frac{FWHM(degrees)}{2}. \tag{1}$$

The relationship of this angle to FWHM($R_\odot$) is therefore

$$\frac{FWHM(R_\odot)}{2} = R\tan\theta, \tag{2}$$

where R is the radius in units of solar radius of the y-pixel value. Using the fact that FWHM(pixels) = 2FWHM(degrees), it follows that

$$FWHM(R_\odot) = 2R\tan(FWHM(pixels)/4), \tag{3}$$

and this formula was used to convert FWHM in pixels to units of solar radius. An example of the full width of the ray at half maximum as a function of distance along the ray is shown in Figure 7 for 2005 September 7, 17:45:49 UT.

The overall picture of the width of the ray as a function of distance and time is shown in Figure 8. In this figure the FWHM of the ray has been averaged over bins 0.1 $R_\odot$ in size in distance along the ray axis. In the first data interval (September 7, 17:04:32 UT - 19:42:54 UT) a steady outward progression of an increasing width can be seen until the ray reaches its maximum width of 0.18 $R_\odot$ at ∼18:15-18:30 UT on September 7 at a distance of $\sim$ 0.8 $R_\odot$ along the ray axis. The second interval (September 8, 00:26:47 UT - 02:30:08 UT) shows a rather constant width at a given distance along the ray axis with a mean width of 0.029 $R_\odot$ and standard deviation of 0.006 $R_\odot$. By the time of the third interval (September 8, 18:17:44 UT - 20:08:43 UT) the larger width of ∼0.11 $R_\odot$ at the base of the ray indicates that the low coronal loop arcade has extended further outward into the field of view of the instrument. The width of the ray beyond the arcade has also decreased in width relative to

the same distance along the ray at the two earlier time intervals; the mean widths (standard deviations) of the ray at a distance of 0.8 $R_\odot$ along the ray were determined to be 0.059, 0.028, 0.019 $R_\odot$ (0.033, 0.012, 0.009 $R_\odot$) for the first, second and third intervals, respectively, indicating a steady decrease in width from the beginning to the end of the observations.

2.2. Extraction of Current Sheet Parameters

For all of our measurements we made the assumption that the CME, ray, etc. were in the plane of the sky and, therefore, no corrections for projection effects were necessary. This is justified by the close proximity to the east limb of the source active region, flare and EPL. The extent of the current sheet can be seen in plots of the full width at half maximum of the ray as a function of distance along the ray axis as shown in Figure 7. It is therefore possible to obtain from such plots a measurement of the p and q parameters of the Lin and Forbes (2000) model corresponding to the arcade top and flux rope base, respectively, as well as the difference, q-p, the current sheet length (Figure 1). An analytical determination of the two end points of the current sheet was performed by fitting intervals of data to the left and right of the inflection regions near the points of interest to a linear function of the distance along the ray. The intersection of the resulting lines was taken to be the value of p or q as indicated in Figure 7 by the magenta and cyan points, respectively. These parameters were also determined by visual inspection of the vignetted images and the locations of p and q indicated by dashed lines in Figure 7. In most cases the agreement between the parameters determined visually and analytically was quite good.

Repeating the measurements of p and q for all images for which such measurements are feasible yields the time dependence of the current sheet geometry. The outward progression of what we consider to be the flux rope base, q could only be followed through the Mk4 field of view until ∼18:01 UT, as shown in the top panel of Figure 9. The reader can view this period in the accompanying Mk4 movie. Prior to making this determination it was necessary to make a time correction for the scan location of the ray. This correction is necessary because the data recorded in each image are taken over 720 scans, each taking 0.25 seconds to perform. Scans commenced at a position angle of 124° over the southeast limb and alternated between clockwise and counter-clockwise in direction. The time correction $\Delta t(s)$ for a feature (pixel) in an image at a position angle θ is, therefore,

$$\Delta t(s) = \begin{cases} 0.5 \times (124^\circ - \theta), & \theta \leq 124^\circ; \\ 0.5 \times (360^\circ - \theta + 124^\circ) & \theta > 124^\circ, \end{cases} \tag{4}$$

for clockwise scans with a similar correction for counter-clockwise scans. With the time

corrections applied to the data, the resulting time dependence of p, q, and q-p were determined as shown in Figure 9 for times near the beginning of the formation of the ray. In each plot shown, the points determined analytically from the non-vignetted images and those determined visually from the vignetted images were combined and fitted to a second order polynomial in time. The coefficients resulting from the fits were used to determine the speed and acceleration as tabulated in Table 1. In each case, the initial speed corresponds to the speed at the time of the first measurement, and the final speed corresponds to the speed at the last time for which q could be measured. The growth rate of the current sheet length was found to increase from 21.97 km/s at 17:42UT to 724.16 km/s at 18:01UT due mainly to the rapid expansion of the flux rope base (0.64 km s^{-2}) relative to the top of the arcade (0.04 km s^{-2}).

Figure 10 shows the time development of the top of the arcade, p, as a function of time for the three intervals of data. The top of the arcade slowly rises with time, increasing by ~ 0.1 $R_\odot$ after 1 day. A portion of this is due to solar rotation. Using a synodic rotation rate (Newton & Nunn 1951) of

$$\omega = 13.39^\circ day^{-1} - 2.7^\circ day^{-1} \sin^2(\lambda), \tag{5}$$

where λ is the heliographic latitude, we estimate the movement of p over a time δt due to solar rotation to be

$$\delta p = p \cos(\lambda)(1 - \cos(\omega \delta t)). \tag{6}$$

For a flare occuring at a latitude λ of South 10° this translates to a change in p of $\sim$0.004 $R_\odot$ over the course of 1 day, i.e. about a 4 percent effect. Therefore most of the ~ 0.1 $R_\odot$ increase in p over one day is due to the rise of the arcade rather than to solar rotation.

At the onset of the ray formation the position angle ψ of the ray axis at 1 $R_\odot$ moved rapidly southward, remaining at $\sim 99.5^\circ$ for several hours as shown in Figure 11. By the third data interval, late on September 8, the ray had moved $\sim 2^\circ$ farther south. We estimate how much of this is due to solar rotation by the relation (Li et al. 2000)

$$\delta\psi = \tan^{-1}\left(\frac{\tan\lambda}{\cos(\omega\delta t)}\right) - \lambda, \tag{7}$$

with ω given by equation 5. The ray axis movement due to solar rotation over the course of 1 day is therefore $\sim 0.25^\circ$, which is relatively minor compared to the observed movement. We think that most of this motion was due to the ray's response to the relaxation of the background coronal magnetic field structure following the CME.

2.3. Observation of Outward Moving Material

One of the interesting features of the ray early in its development is the appearance of a large structure that grows in size with time and then rapidly exits the field of view. The structure can be seen in Figure 8 forming around 18:00 UT, increasing in width with time and moving outward along the ray axis. Shown in Figure 12 are the FWHM of the ray as a function of the distance along the ray at four different times that illustrate the changing nature of this structure. It first appears at 17:57:35 UT as a small bump near $\sim$0.25 $R_\odot$ and with a maximum FWHM of $\sim$0.05 $R_\odot$. Approximately six minutes later it has grown to a FWHM of $\sim$0.07 $R_\odot$ and moved out along the ray axis to $\sim$0.35 $R_\odot$. At 18:12:22 UT it has reached a FWHM of $\sim$0.09 $R_\odot$ without much outward movement. Three minutes later it has moved out to the point that its full extent cannot be observed.

The radial FWHM of this feature was fitted to a Gaussian function over the region of the structure at each time for which the structure could be observed in its entirety. The resulting centroid and FWHM of each fit are shown in Figure 13. The location of the centroid of the structure is seen to be fairly linear while the width of the structure expands quadratically with time. A second order polynomial fit was applied to these results, yielding the kinematic quantities shown in Table 2. The centroid of the structure is determined to move outward with an average speed of 80.47 km/s while its radial width accelerates at the rate of 0.208 km/s^2. Shown in Figure 14 are vignetted Mk4 white light polarization brightness images for the times corresponding to those of Figure 12. The outward expanding feature is difficult to discern in these images.

The physical significance of this structure is not clear; perhaps it is merely the twisting of the ray or the plane of the ray as it develops, or it is a dynamic feature associated with the reconnection site. It might also be associated with the reconnection diffusion region, but since no Sunward flows were observed at any time, the location of the diffusion region as identified by the X-point is unclear. Since the CS itself is not clearly defined until $\sim$ 18:30 UT, the observed structure may be nothing more than the outward flow of material below the base of the flux rope prominence. More observations of such outward moving structures will be needed to determine their nature.

2.4. Oscillatory Nature of the Ray Position Angle

Another interesting aspect of the ray morphology observed in the time dependence of the position angle of the ray axis at the surface of the Sun is an apparent oscillation early on in the development of the ray as shown in Figure 15. The oscillatory nature observed is

reminiscent of another wave phenomenon that manifests itself during a CME, namely the behavior of streamers driven by waves associated with coronal mass ejections (Chen et al. 2010). CMEs frequently cause streamer disruptions. Usually such interactions cause the apparent deflection of a pre-existing streamer (e.g., Hundhausen et al. 1987; Sheeley et al. 2000). In most CME-driven deflections, the streamer moves to another position but does not oscillate. As was pointed out by Chen et al. (2010), the streamer belt existing at the time of the 2004 July 5 23:06 UT and 2004 July 6, 20:06 UT CMEs was pushed aside from its equilibrium position when the CMEs progressed outward and the streamers exhibited large-scale, sinusoidal wavelike motions. This same behavior was likewise observed during the 2005 September 7 CME. Prior to the CME, streamers were observed at position angles of $\sim 50°$ and $\sim 130°$ on the east limb and, $\sim 260°$, and $\sim 290°$ on the west limb. As the CME lifted off from the Sun's surface, the two streamers closest to the location of the CME were pushed away from the CME lift-off point to $\sim 30°$, $\sim 150°$. The other streamers, on the west limb of the Sun oscillated a small amount, but nevertheless appear to have experienced a force suggestive of an MHD wave traveling around the Sun shortly after the emergence of the CME.

In an effort to quantify the oscillation of the ray along its axis, a fit of the data to a damped harmonic oscillator with a time-dependent frequency was performed. Specifically, the position angle of the ray at 1 $R_\odot$ was fit to the function of time t

$$Ae^{-kt}\cos(\omega t + \delta) + C, \tag{8}$$

where A is the amplitude of the oscillation, k is a decay constant, ω is the angular frequency, δ is a phase factor, and C is a constant. The angular frequency is given by

$$\omega = \omega_0 e^{-\lambda t}, \tag{9}$$

where ω_0 is a constant and λ is a frequency decay factor. In order to keep the number of fitting parameters to a minimum, the decay factors were fixed at $k = 1.5$ hour^{-1} and $\lambda = 0.1$ hour^{-1}. The resultant fit, shown as a solid red line in Figure 15, produced an amplitude $A = -0.9°$, and an initial angular frequency of $\omega_0 = 12$ rad/hour corresponding to a period of $\sim$0.5 hour.

While the exact form of the function describing the motion of the ray axis is unknown, the fit parameters give an estimate of the period of the oscillation which is not inconsistent with the period of 1 hour determined for the streamer waves reported by Chen et al. (2010). Nevertheless, the physical interpretation of the oscillation observed for the ray axis may not necessarily be attributed to the same force causing the streamer waves, which the authors attribute to a magnetohydrodynamic kink mode. Deflections of streamers by CMEs are the

result of fast-mode waves across the magnetic field produced by CMEs moving through the corona (Hundhausen et al. 1987). But both the ray axis oscillation and streamer waves have as their primary cause the occurrence of a CME.

3. Discussion and Conclusions

We have determined some of the basic parameters describing the morphology of a bright ray as it formed in the wake of the CME of 2005 September 7. Using the non-vignetted white-light images acquired by the Mk4 K-Coronameter at the MLSO, the width of the ray was determined along its axis over a height range of 1.08 to 2.16 $R_\odot$ from the time when the measurements were first possible at 17:39 UT on September 7 until 20:08 UT on September 8. The narrowest width observed was $\sim$0.01 $R_\odot$ ($\sim$7 x 10^3 km) as determined from fits of the image pixel intensities to a Gaussian plus quadratic background term. More typically the ray width was $\sim$0.04 $R_\odot$, or 3×10^4 km (all our measurements assume projection on the plane of the sky). We found that the width of the ray was narrowest near its base and widened with height and time (Figures 3, 8, and 12).

These widths can be compared with post-CME current sheet widths measured in other studies at different wavelengths and heights. For 27 SMM CME CSs Webb et al. (2003) found a mean width of 0.10 $R_\odot$ at a mean height of 1.2 $R_\odot$. More recently, Vršnak et al. (2009) measured mean widths of 0.26 $R_\odot$ at similar heights for 3 LASCO WL events, and reported UV spectroscopic results for CS widths of 6 events from 0.1-0.3 $R_\odot$ at similar heights. Most of these spectroscopic results on CME CSs come from SOHO UVCS observations of hot Fe XVIII emission. At heights of 4-5 $R_\odot$ the CS widths more than doubled, ranging from 0.4 to 0.9 $R_\odot$ in both WL and the UV. However, possibly the only other comparable measurement to ours at this low coronal height is that made by Savage et al. (2010) for the CS associated with the famous "Cartwheel CME" of 2008 April 8-9. They analyzed Hinode XRT images in soft X-rays which extended down to the solar surface and thus were able to view the CS all the way down to the loop arcade. They found a mean CS width of $4 - 5 \times 10^3$ km at heights of only 0.1-0.2 $R_\odot$, just above the loop arcade and the p point. Considering the instrumental differences, it is remarkable that our WL CS width is only slightly larger than this X-ray CS width at similar or slightly larger heights. Also the 2005 September 7 CME was very fast whereas the Cartwheel CME speed was only moderate, $\sim$450 km/s.

The Lin and Forbes (2000) model parameters describing the current sheet were determined analytically from computation of inflection points in the ray width as well as from visual inspection of the vignetted images. The motion of the top of the current sheet (q) was measured as it proceeded outward from 0.27 $R_\odot$ to 0.89 $R_\odot$. A fit of q to a 2nd order

polynomial in time yielded a final speed of 780 km/s with an acceleration of 0.64 km/s^2. A similar treatment of the top of the arcade resulted in a final speed of 54 km/s with an acceleration of 0.04 km/s^2. The current sheet length was determined to have a final speed of **724** km/s, an acceleration of **0.62** km/s^2 , and an average growth rate of **373** km/s as it grew from 0.13 $R_\odot$ to 0.74 $R_\odot$ in length. This is the first time that measurement of a post-CME current sheet has been made in WL over its entire length, ie., between the upper and lower "Y" points in many reconnection flare models. Savage et al. (2010) also were able to measure q and p values using XRT X-ray and LASCO white light observations. They found results for the speed of q and the growth of the CS similar to those of Webb et al. (2003) of a few hundred km/s. We obtained higher speeds for the September 2005 event, not surprising since the CME frontal speed was much higher than those of the events described by Webb et al. (2003) and Savage et al. (2010).

The reconnection rate in a current sheet is prescribed by the Alfvén Mach number, M_A. Many loss-of-equilbrium CME models, such as Lin and Forbes (2000) and Linker et al. (2001), assume a constant M_A of about 0.1. According to the Sweet-Parker theory (Parker 1957), the Mach number is related to the current sheet parameters as

$$M_A = width/(q - p). \tag{10}$$

Using our average width and the q-p results above, we find $M_A = 0.070$. Although smaller than M_A used in some models, our value is consistent with other WL and UV CS results such as Yokoyama et al. (2001), Lin et al. (2005; 2007), Ciaravella and Raymond (2008) and Vršnak et al. (2009). However, Savage et al. (2010) find a much smaller range of 0.002 - 0.006.

In the September 2005 event the ray moved rapidly poleward, $> 2.5°$, during the first half hour then remained relatively stationary (Figure 11). Webb et al. (2003) observed lateral motions in about half of their CME-rays, and such motions are frequently observed for SOHO rays, sometimes over tens of degrees in PA. The southward drift of the ray in the Savage et al. (2010) event amounted to 25° at a rate of 4°/hr. Likewise in the fast 2003 November 18 and 2002 January 8 events studied by Lin et al. (2005) and Ko et al. (2003), respectively, the rays slowly moved poleward over 26 and 20 degrees, respectively. These motions are likely related to varying viewing geometry as well as adjustments between the eruptive and the background magnetic fields as the CME moves outward.

No evidence was seen in this event of the outward motion of the X-type reconnection point connecting the arcade and flux rope (Webb et al. 2003). Its absence may be due to the diffusion region possibly forming and dissipating on a time scale shorter than the image cadence. Nevertheless, a number of other interesting features were observed. A large structure moving outward was observed early on in the development of the ray having an

unknown physical significance but possibly related to the diffusion region. The position angle of the ray axis at 1 $R_\odot$ had an oscillatory nature and was determined to have a period of ∼0.5 hour, consistent with the period of streamer waves observed during the CMEs of 2004 July 5, 23:06 UT and 2004 July 6, 20:06 UT (Chen et al. 2010), although not necessarily attributed to the same wave phenomenon.

Future work will focus on deriving density distributions of the ray for comparisons with reconnection models and the results of other post-CME ray studies.

A.G.L. acknowledges support from AFRL Contract FA8718-05-C-0036, and D.F.W. acknowledges support from AFRL contracts AF19628-00-C-0073 and FA8718-06-C-0015 and Navy NRL grant N00173-01-1-G013. We gratefully acknowledge the image data provided courtesy of the Mauna Loa Solar Observatory, operated by the High Altitude Observatory, as part of the National Center for Atmospheric Research (NCAR). NCAR is supported by the National Science Foundation.

REFERENCES

Asai, A., Yokoyama, T., Shimojo, M., & Shibata, K. 2004, ApJ, 605, L77

Bemporad, A., Poltetto, G., Suess. S.T., Ko, Y.-K., Schwadron, N.A., Elliott, H.A., & Raymond, J.C. 2006, ApJ, 638, 1110

Chen, Y., Song, H.Q., Li, B., Xia, L.D., Wu, Z., Fu, H., & Li, X. 2010, ApJ, 714, 644

Chen, P.F. 2011, Sol. Phys., 8, lrsp-2011-1,http://www.livingreviews.org/lrsp-2011-1

Ciaravella, A., Raymond, J.C., Li, J., Reiser, P., Gardner, L.D., Ko., Y,-K., & Fineschi., S. 2002, ApJ, 575, 1116

Ciaravella, A., Raymond, J.C., van Ballegooijen, A., Strachan, L., Vourlidas, A., Li, Chen, J., & Panasyuk, A. 2003, ApJ, 597, 1118

Ciaravella, A., & Raymond, J.C. 2008, ApJ, 686, 1372

Ciaravella, A., Webb, D.F., Giordano, S., & Raymond, J.C. 2013, ApJ, in press

Cliver, E.W. 1989, Sol. Phys., 122, 319

Elmore, D.F, Burkepile, J.T., Darnell, J.A., Lecinski, A.R., & Stanger, A.L. 2003, in *Polarimetry and Astronomy, Proc. of the SCIE*, ed. S. Fineschi, 4843, 66

Fisher, R.R., Lee, R.H., MacQueen, R.M, and Poland, A.I. 1981, Applied Optics, 20, 1094

Hiei, E., Hundhausen, A.J., & Sime, D.G. 1993, Geophys. Res. Lett., 20, 2785

Hundhausen, A.J., Holzer, T.E., & Low, B.C. 1987, J. Geophys. Res., 92, 11173

Illing, R.M.E., & Hundhausen, A.J. 1986, J. Geophys. Res., 91, 10951

Innes, D.E., McKenzie, D.E., & Wang, T. 2003, Sol. Phys., 217, 267

Kahler, S.W., & Hundhausen, A.J. 1992, J. Geophys. Res., 97, 1619

Ko, Y.-K., Raymond, J.C., Lin, J., Lawrence, G., Li, J., & Fludra, A. 2003, ApJ, 594, 1068

Kohl, J.L., Noci, G., Cranmer, S.R., & Raymond, J.C. 2006, Astron. Astrophy. Rev., 13, 31

Li, J., Jewitt, D., & LaBonte, L. 2000, ApJ,539, L67

Lin, J., & Forbes, T.G. 2000, J. Geophys. Res., 105, 2375

Lin, J. 2004, Sol. Phys., 219, 169

Lin, J., Ko, Y.-K., Sui, L., Raymond, J.C., Stenborg, G.A., Jiang, Y., Zhao, & Mancuso, S. 2005, ApJ, 622, 1251

Lin, J., Li, J., Forbes, T.G., Ko, Y.-K., Raymond, J.C. & Vourlidas, A. 2007, ApJ, 658, L123

Linker, J.A., Lionell, R., Mikic, Z., & Amarik, T. 2001, J. Geophys. Res., 106, 25,165

McComas, D.J., Phillips, J.L., Hundhausen, A.J., & Burkepile, J.T. 1991, Geophys. Res. Lett., 18, 73

McKenzie, D.E., & Hudson, H.S. 1999, ApJ, 519, L93

Newton, H.W., & Nunn, M.L. 1951, M.N.R.A.S., 111, 413

O'Dwyer, B., Del Zanna, G., Mason, H., Weber, M.A., & Tripathi, D. 2010, Å, 521, A21

Parker, E.N. 1957, J. Geophys. Res., 62, 509

Raymond, J.C., Ciaravella, A., Dobrzycka, D., Strachan, L., Ko, Y.-K., Uzzo, M., & Raouafi, N.-E. 2003, ApJ, 597, 1106

Reeves, K.K., & Golub, L. 2011, ApJ, 727, L52

Riley, P., Linker, J.A., Mikic, Z., Odstrcil, D., Pizzo, V.J., & Webb, D.F. 2002, ApJ, 578, 972

Saint-Hilaire, P., Krucker, S., & Lin, R.P. 2009, ApJ, 699, 245

Savage, S.L., McKenzie, D.E., Reeves, K.K., Forbes, T.G., & Longcope, D.W. 2010, ApJ, 722, 329

Savage, S.L., McKenzie, D.E., & Reeves, K.K. 2012, ApJ, 747, L40

Sheeley, N.R.,Jr., Hakala, W.N., & Wang, Y.M. 2000, J. Geophys. Res., 105, 5081

Sheeley, N.R., Jr., Warren, H.P., & Wang, Y.-M. 2004, ApJ, 616, 1224

Sheeley Jr, N.R., & Wang, Y.-M. 2007 ApJ, 655, 1142

Shibata, K., et al. 1995, ApJ, 451, L83, 1995

Shibata, K. 1999, Astrophys. Space Sci., 264, 129

Simnett, G.M. 2004, Å, 416, 759

Solar-Geophysical Data Comprehensive Reports, 739 Part II, 4, March 2006, H.E. Coffey, ed.,U.S. Department of Commerce (Boulder, CO, USA 80303)

St. Cy, O.C., Plunkett, S.P., Michels, D.J., Paswaters, S.E., Koomen, M.J., Simnett, G.M., Thompson, B.J., Gurman, J.B., Schwenn, R., Webb, D.F., Hildner, E., & Lamy, P.L. 2000, J. Geophys. Res., 105, 18169

Sui, L., & Holman, G.D. 2003, ApJ, 596, L251

Sui, L., Holman, G.D., White, S.M., & Zhang, J. 2005 ApJ, 633, 1175

Švestka, Z.F., Fontenla, J.M, Machado, M.E., Martin, S.F., & Neidig, D.F. (1987), Sol. Phys., 108, 237

Švestka, Z., & E. W. Cliver 1992, History and basic characteristics of eruptive flares, in *Eruptive Solar Flares*, ed. Z. Svestka, B. Jackson, & M. Machado, (Springer-Verlag, New York), 1

Vršnak, B., Poletto, G., Vujić, E., Vourlidas, A., Ko, Y.-K., Raymond, J.C., Ciaravella, A., Žic, T., Webb, D.f., Bemporad, A., Landini, F., Schettino, G., Jacobs, C., & Suess, S.T. 2009, Å, 499, 905,doi:10.1051/0004-6361/200810844

Wang, T., Sui, L., & Qiu, J. 2007, ApJ, 661, L207

Warren, H.P., O'Brien, C.M, & Sheeley, N.R., Jr. 2011, ApJ, 742, 92

Webb, D.F., & Cliver, E.W. 1995, J. Geophys. Res., 100, 5853

Webb, D.F., Burkepile, J., Forbes, T.G., & Riley, P. 2003, J. Geophys. Res., 108(A12) 2003

Yokoyama, T., Akita, K., Morimoto, T., Inoue, K., & Newmark, J. 2001, ApJ, 546, L69

Table 1. Kinematics of the early development of the post-CME ray of 2005 September 7.

Ray Feature	Initial Speed (km s^{-1})	Final Speed (km s^{-1})	Acceleration (km s^{-2})	Average Speed (km s^{-1})
Flux Rope Base (q)	52.67	780.15	0.64	416.41
Top of Arcade (p)	6.04	53.64	0.04	29.84
Current Sheet Length (q-p)	21.97	724.16	0.62	373.06

Table 2. Kinematics of the outward moving structure observed early in the development of the post-CME ray of 2005 September 7.

Structure Characteristic	Initial Speed (km s^{-1})	Final Speed (km s^{-1})	Acceleration (km s^{-2})	Average Speed (km s^{-1})
Centroid	84.29	76.65	-0.009	80.47
FHWM	-0.52	184.41	0.208	91.95

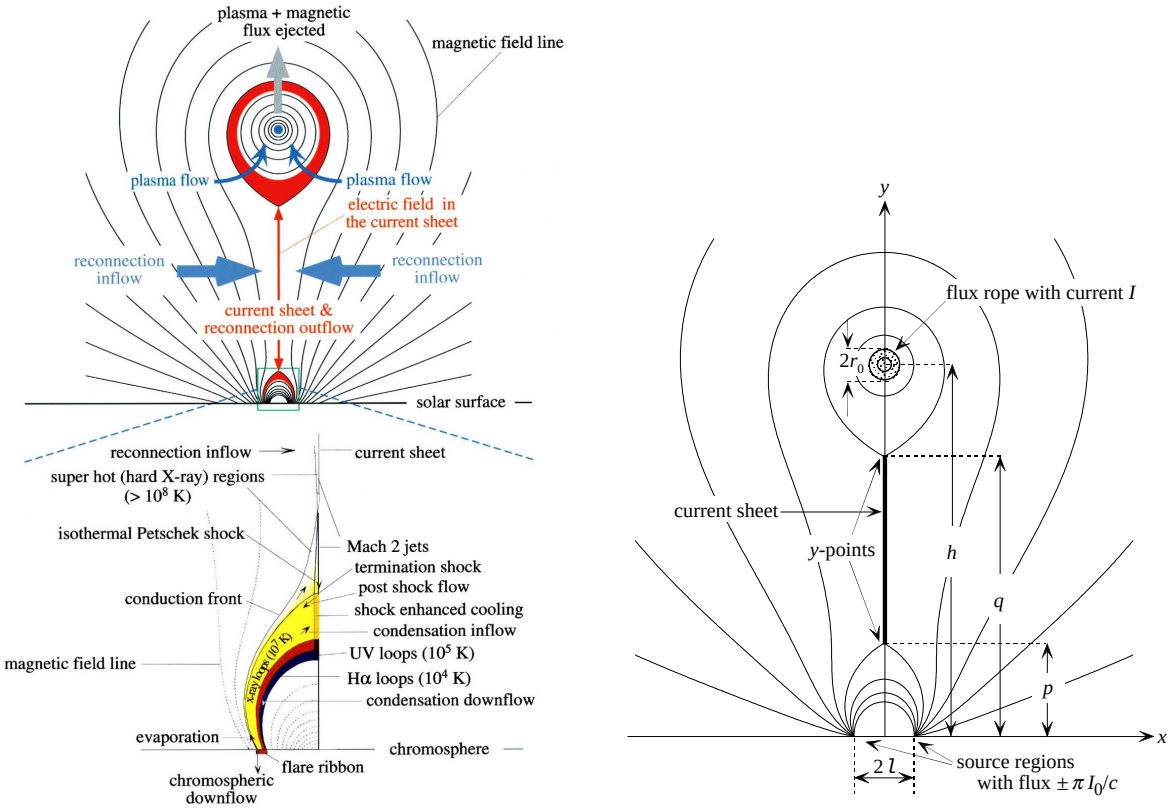

Fig. 1.— *Left*) Schematic of the disrupted magnetic field that forms during a coronal mass ejection. Catastrophic loss of equilibrium, occurring in a magnetic configuration including a flux rope, stretches the closed field creating a "Kopp-Pneuman"-type structure. From Lin (2004). *Right*) Diagram of the erupting flux rope model of Lin and Forbes (2000). The flux rope is driven upward because of a loss of equilibrium due to two point sources at the base moving toward each other. Reconnection leads to a vertical current sheet, which, at any given time, extends from the Y-shaped points at the top of a growing arcade, $y = p$, to the base of the flux rope, $y = q$.

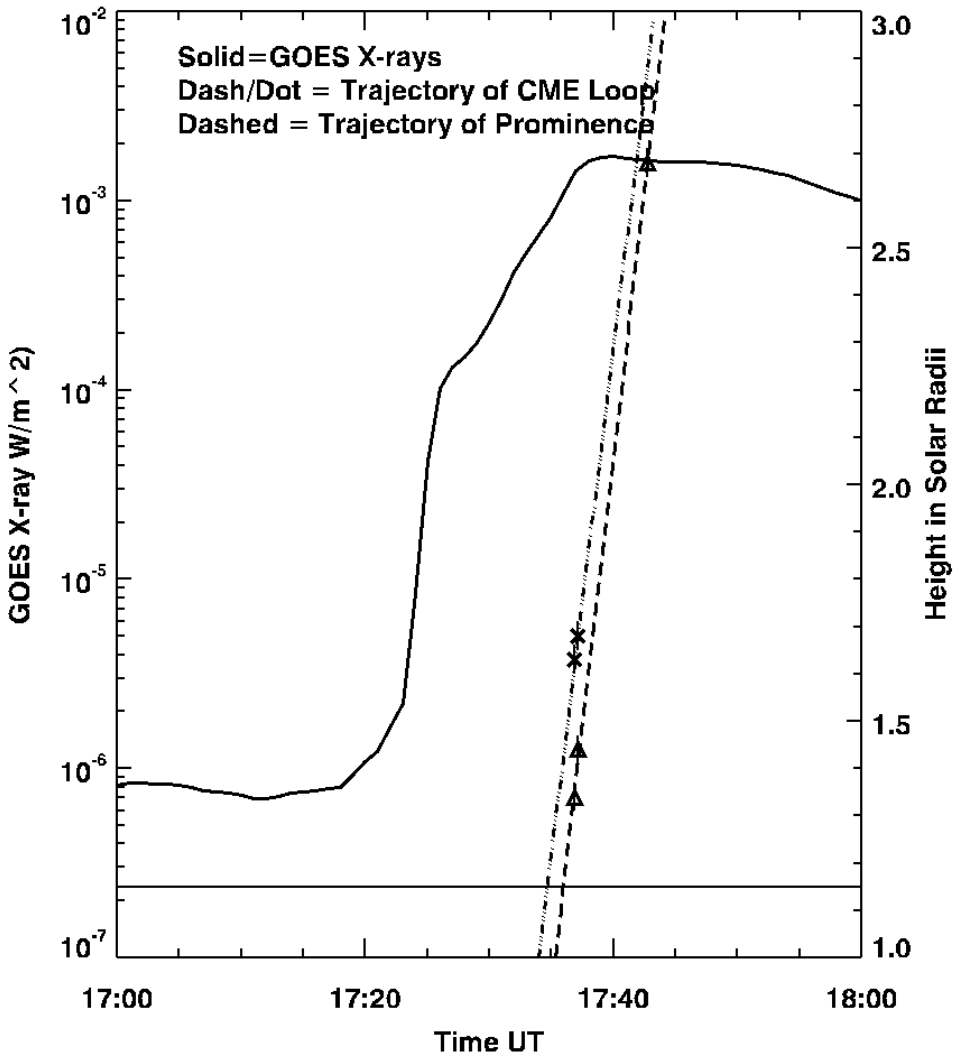

Fig. 2.— Height-time measurements of the loop leading edge of the CME observed at 17:36:54 and 17:37:08 UT and of the prominence structure observed at 17:36:54, 17:37:08, and 17:42:45 UT, superposed on the GOES 1-8 A X-ray light curve. The GOES emission log scale is on the left axis and the Mk4 linear height scale on the right axis. The horizontal line is at the location of the Mk4 occulting disk; 1.0 $R_{\odot}$ is the solar limb.

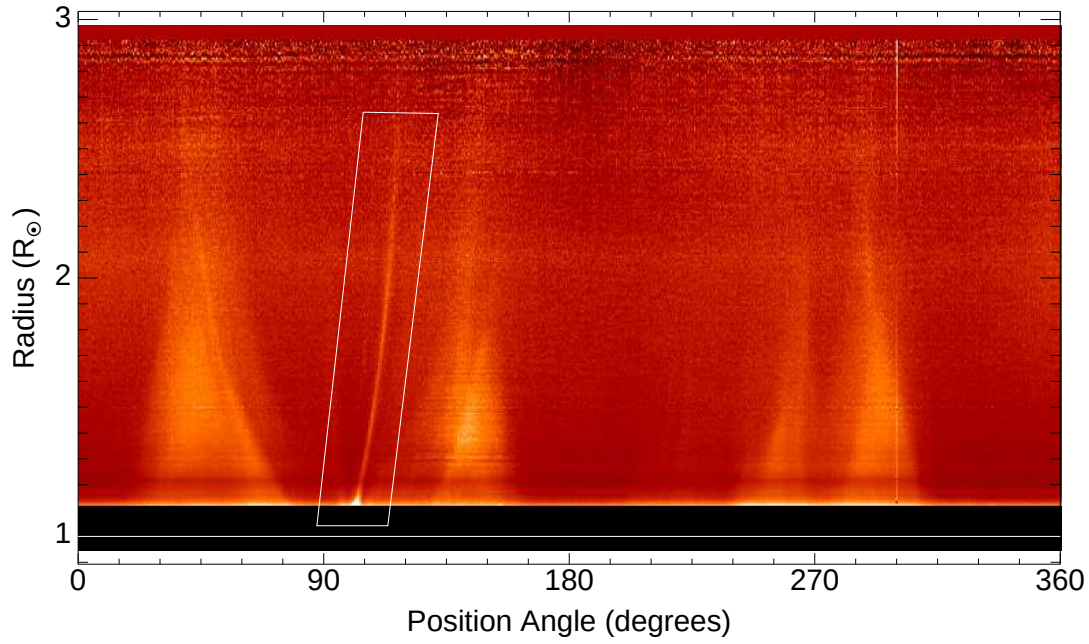

Fig. 3.— Example of selecting data for analysis from a vignetted Mk4 white light polarization brightness image in polar coordinates. The white 4-sided polygon indicates the region of the image used in the analysis. This image is for 7 September at 19:16:30 UT.

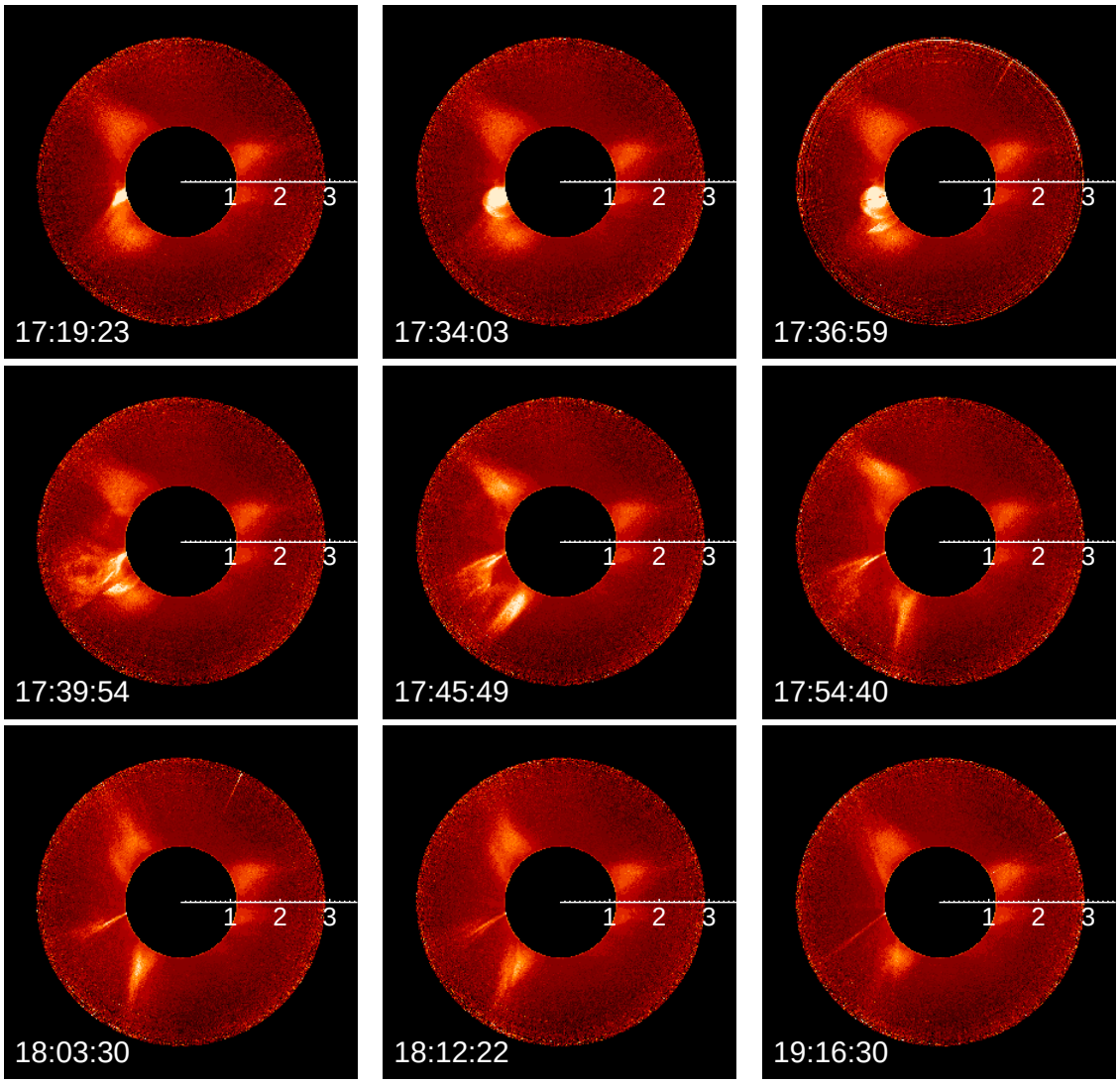

Fig. 4.— The Mk4 white light vignetted data in rectangular coordinates showing the progression of the CME and its trailing ray on 7 September 2005. The observation times (UT) are indicated on the images. The first image, at 17:29:23 UT, shows the pre-event corona. The axes in units of $R_{\odot}$ are shown on the right side of each image and are centered on the Sun.

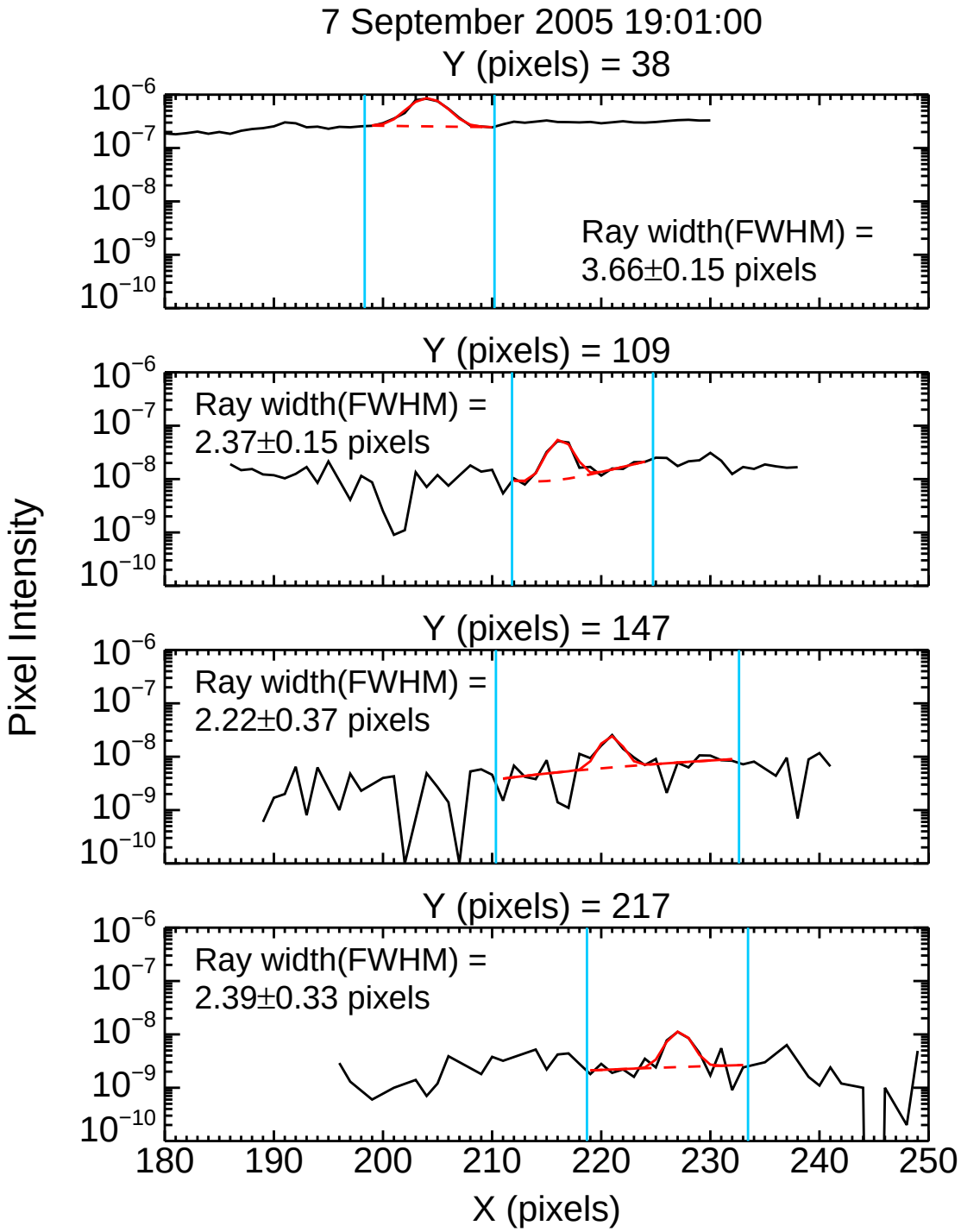

Fig. 5.— The pixel intensity as a function of x-pixel values at constant y-pixel values of **38** (1050″ or 1.1 $R_\odot$), 109 (1395″ or 1.46 $R_\odot$), 147 (1579″ or 1.66 $R_\odot$), and 217 (1919″ or 2.01 $R_\odot$) for the non-vignetted image of 7 September at 19:01 UT. Only data (solid black line) for x-pixels contained inside the 4-sided polygon used to isolate the ray are shown. A fit of the data to a Gaussian plus quadratic background (solid red line) over the interval between the vertical blue lines is shown with the quadratic component indicated (dashed red line).

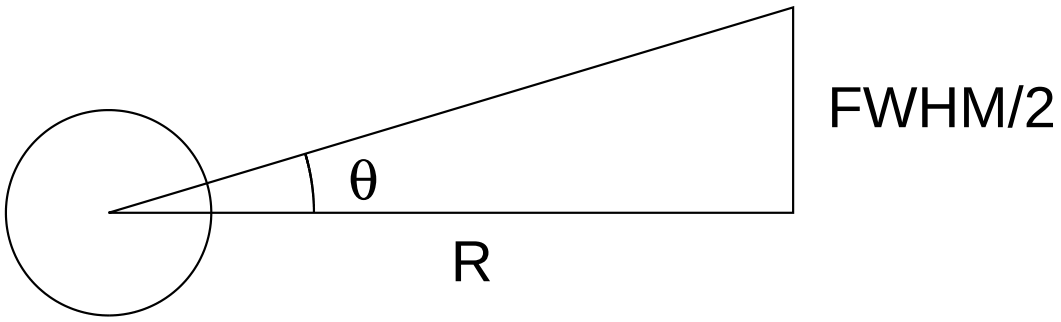

Fig. 6.— The geometry of the ray. R is the radius of the y-pixel value and FWHM is the full width at half-maximum or width of the ray.

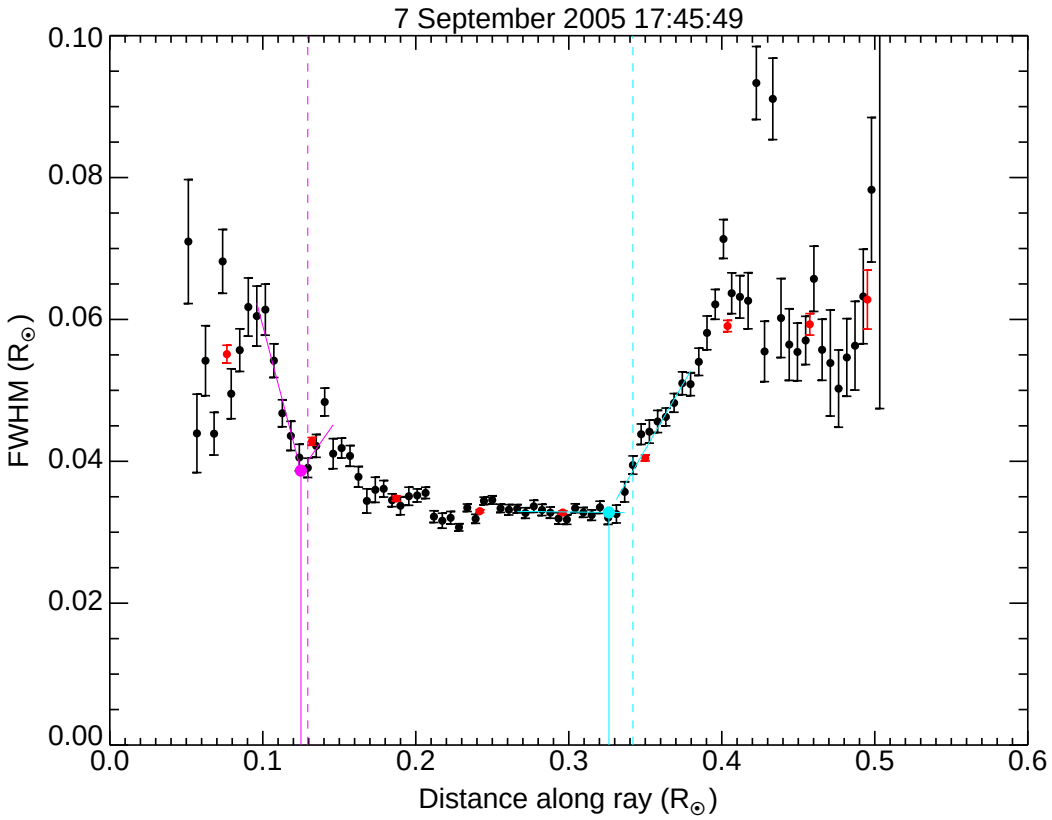

Fig. 7.— The full width of the ray at half maximum (FWHM), determined from Gaussian plus quadratic background fits of the pixel intensity to x-pixel value, as a function of distance along the ray axis (black points) for the image of 7 September at 17:45 UT. The red points denote averages over 10 neighboring points. The magenta and cyan solid lines are the analytically determined locations of the p and q parameters, respectively, as described in the text. The magenta and cyan dashed lines denote the locations of p and q as determined by visual inspection of the vignetted images.

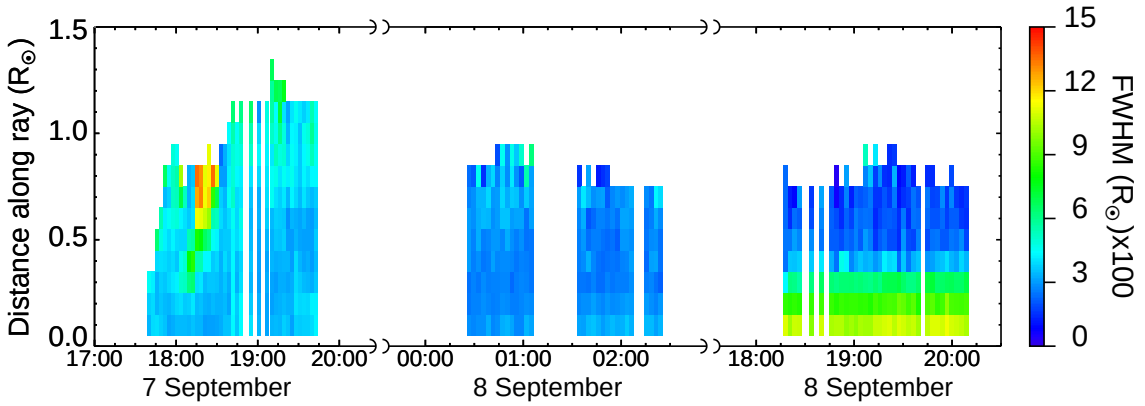

Fig. 8.— The FWHM of the ray shown color-scaled as a function of the distance along the ray with time.

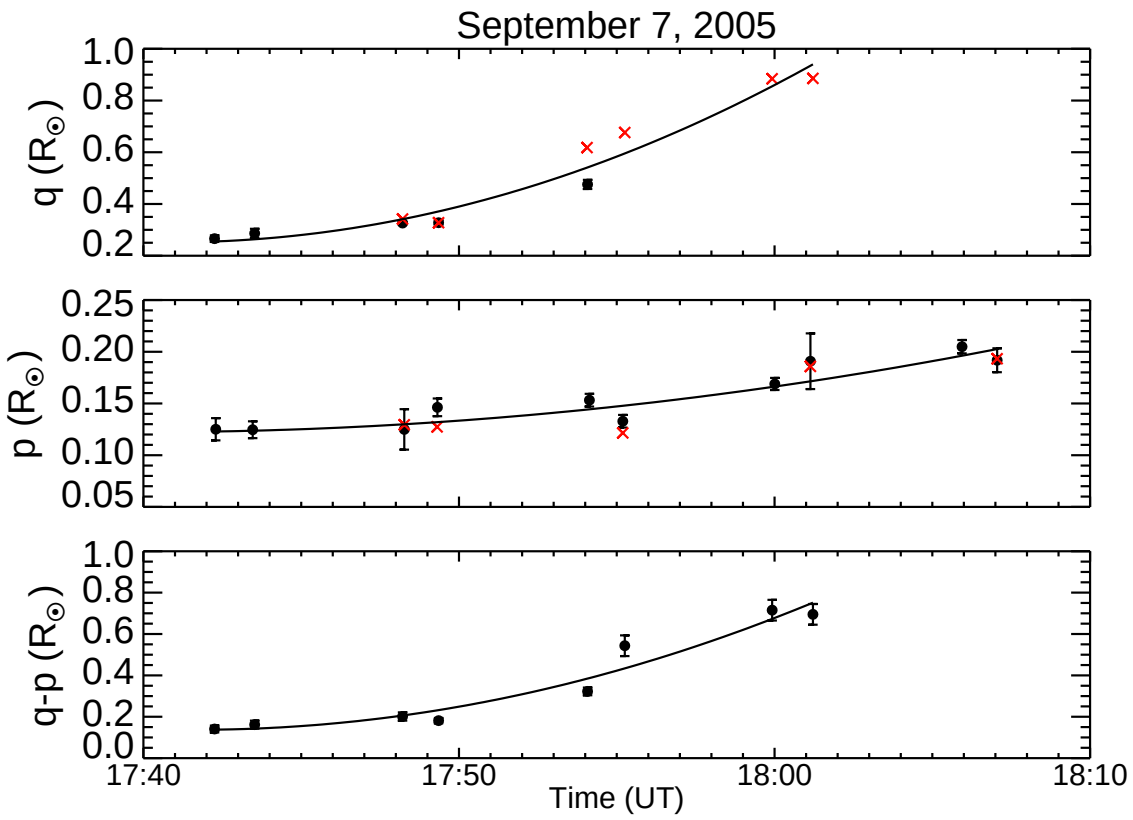

Fig. 9.— The time dependence of (*top*) the base of the flux rope, q, (*middle*) the top of the arcade, p, and (*bottom*) the current sheet length, q-p, early in the development of the ray. In each plot, the measurements determined analytically are shown as black circles and those points determined through visual inspection of the vignetted images are shown as red crosses. The solid black lines are 2nd order polynomial fits to the data.

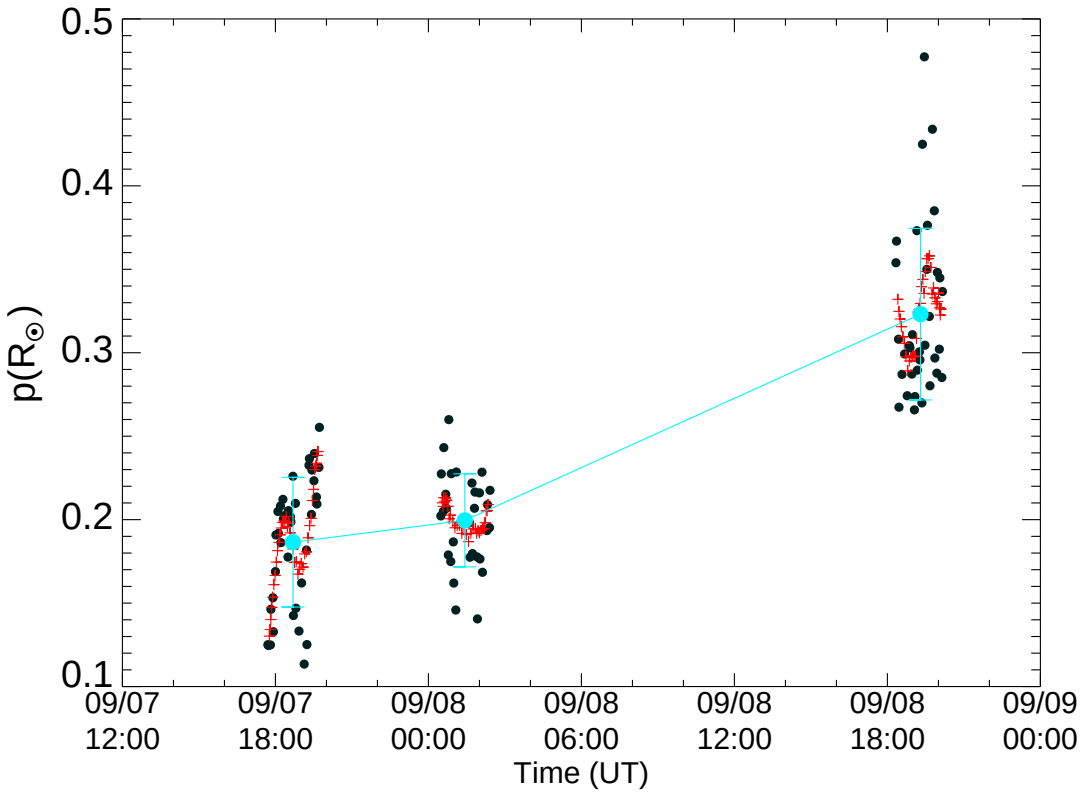

Fig. 10.— The time dependence of the rise of the top of the reforming arcade, p, over ∼1 day. The black points are the data, the red crosses are boxcar averages of width 11, and the connected blue circles are the means of each of the three intervals. The measurements late on September 7 are affected by the fast CME rise. There is an increase of ∼**0.1** $R_\odot$ over ∼1 day, more than expected from solar rotation alone.

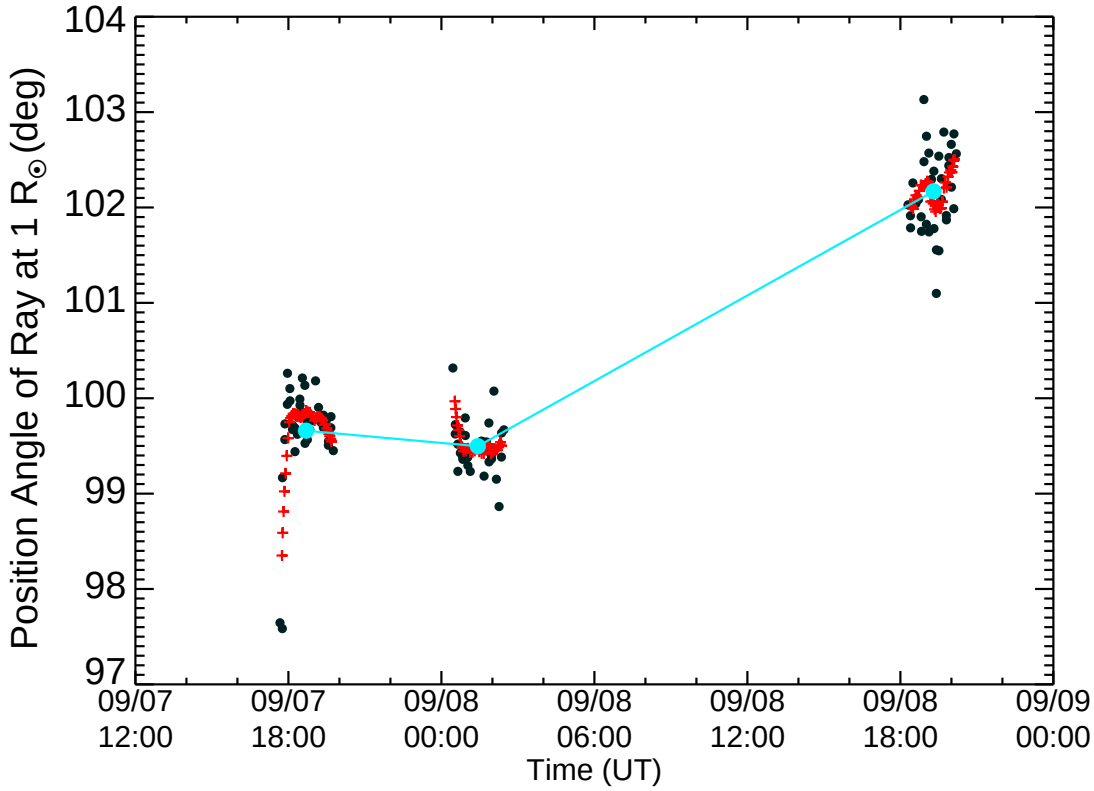

Fig. 11.— The time dependence of the change in PA of the ray axis at 1 $R_\odot$ over ∼1 day. The black points are the data, the red crosses are boxcar averages of width 11, and the connected blue circles are the means of each of the three intervals. As is often observed with fast SOHO CMEs, the ray axis initially moved rapidly southward (poleward) and then remained at $\sim 99.5°$. By late on September 8 the ray had moved $\sim 2°$ farther southward, only part of which is due to solar rotation.

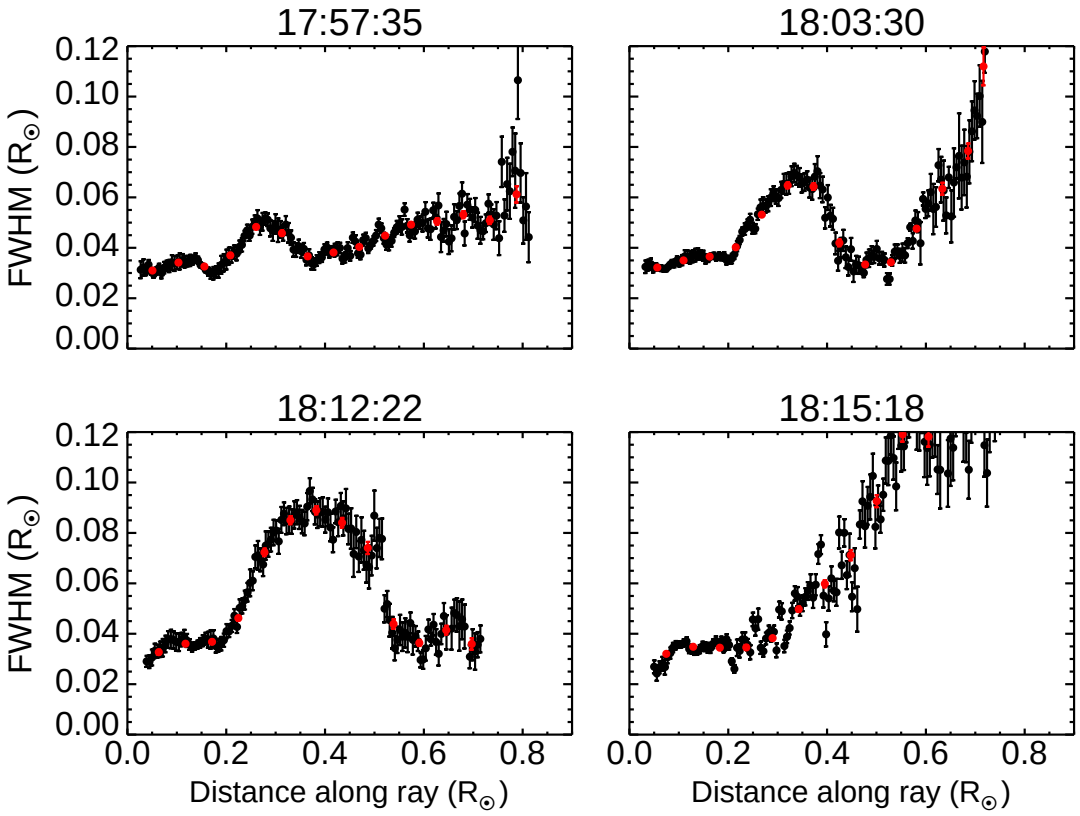

Fig. 12.— The FWHM, determined from Gaussian plus quadratic background fits of the pixel intensity to x-pixel value, as a function of distance along the ray axis (black points) at the times indicated on the plots for 7 September. The red points denote averages over 10 neighboring points.

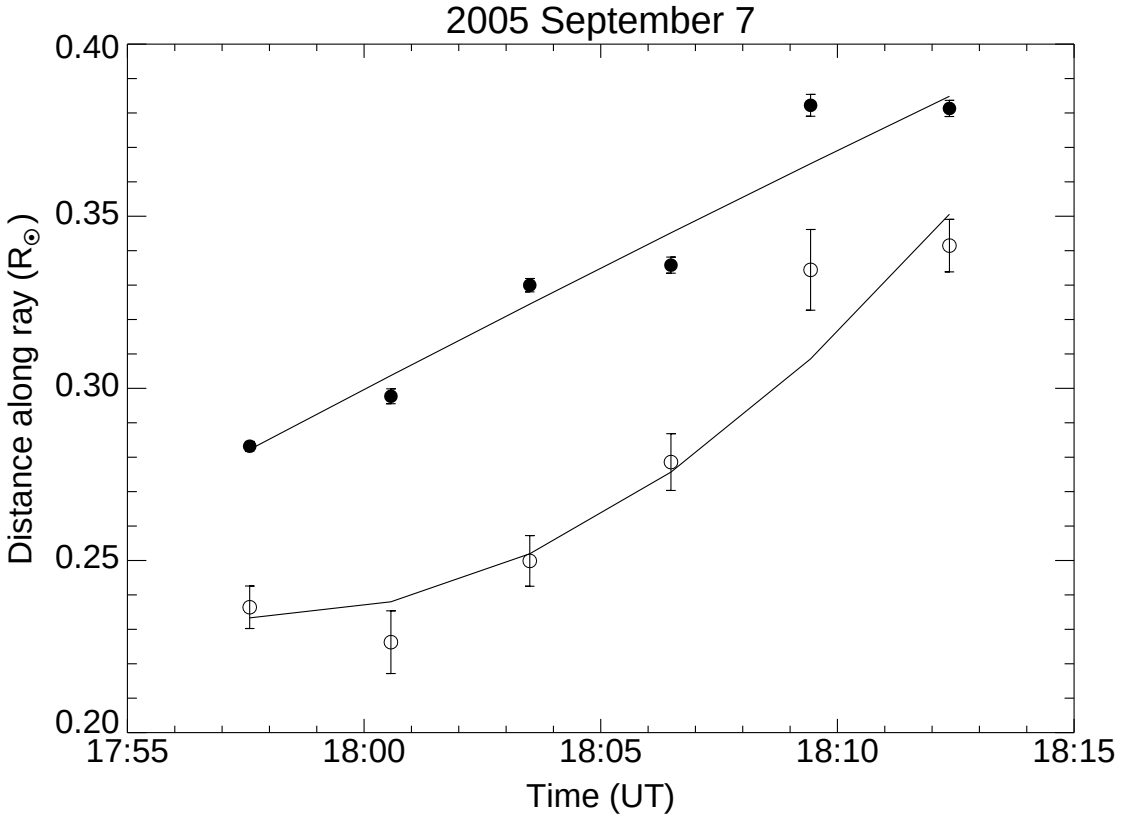

Fig. 13.— The results of fitting to a Gaussian function the outward expanding structure observed in the early development of the ray. The filled circles are the centroids of the structure and the open circles are the FWHM determined from the Gaussian fits. Second order polynomial fits to the respective points are indicated with solid lines.

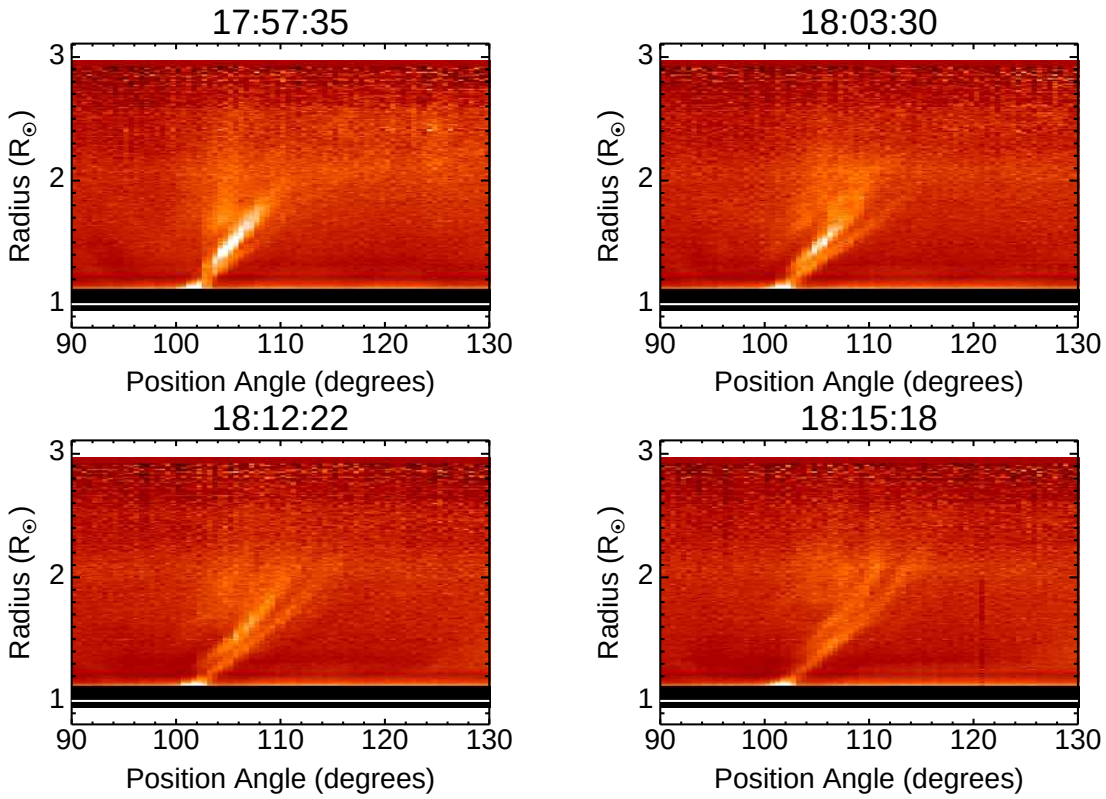

Fig. 14.— Vignetted Mk4 white light polarization brightness images in polar coordinates for the times for the times corresponding to the plots of 12.

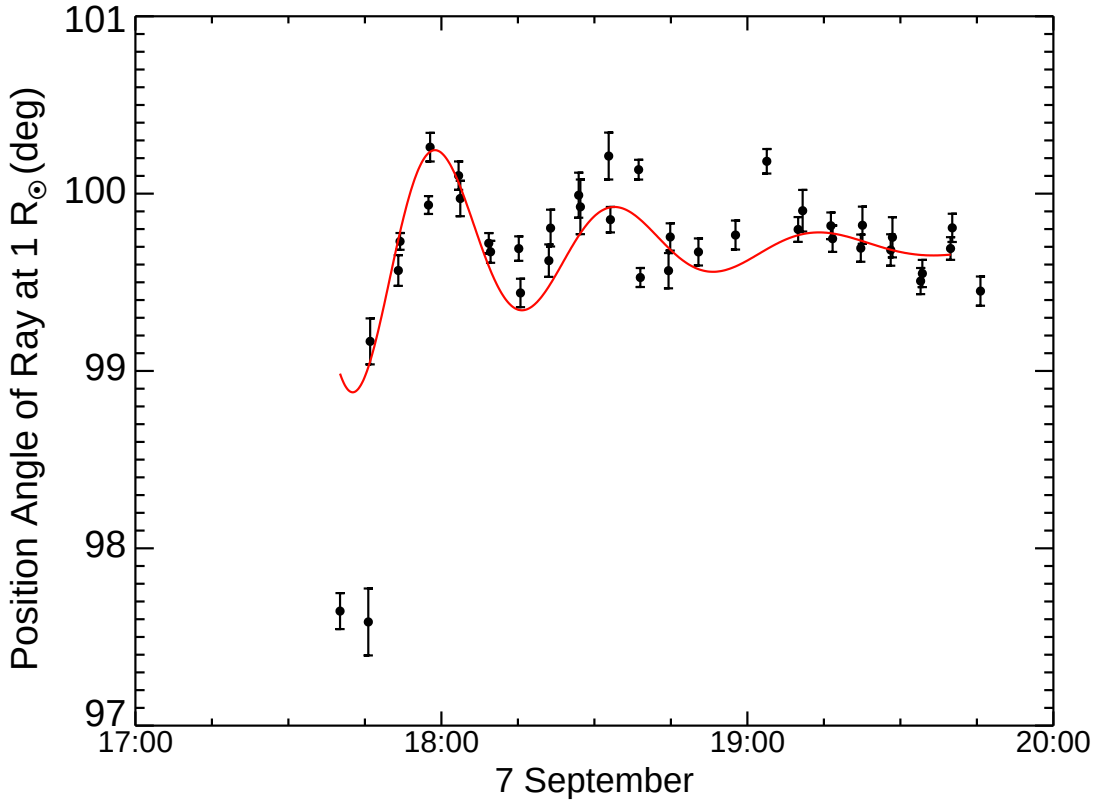

Fig. 15.— The time dependence of the position angle of the ray at 1 $R_\odot$ early in the development of the ray. The red line is a fit of the points to a decaying oscillating function as described in the text.